Revision 1

Wave vector and field vector orientation dependence of Fe K pre-edge X-ray absorption features in clinopyroxenes

Cody J. Steven[1], M. Darby Dyar[1,2], Molly McCanta[3], Matthew Newville[4], and Antonio Lanzirotti[4]

[1]Planetary Science Institute, Tucson, Arizona 85719-2395, U.S.A.

[2]Department of Astronomy, Mount Holyoke College, South Hadley, Massachusetts 01075, U.S.A.

[3]Department of Earth and Planetary Sciences, University of Tennessee, Knoxville, Tennessee 37996, U.S.A.

[4]Center for Advanced Radiation Sources, University of Chicago, 5640 S. Ellis Avenue, Chicago, Illinois 60637, U.S.A.

This is the peer-reviewed, final accepted version for American Mineralogist, published by the Mineralogical Society of America.
The published version is subject to change. Cite as Authors (Year) Title. American Mineralogist, in press.
DOI: https://doi.org/10.2138/am-2022-8547. http://www.minsocam.org/

Abstract

Pre-edge X-ray absorption features are commonly used to derive redox states for transition metal oxides in crystals and glasses. Several calibrations for Fe^{2+} and Fe^{3+} in silicate glasses have utilized the general relationships among pre-edge peak intensity, energy, and redox state. However, absorption variations complicate those relationships in anisotropic crystals. Although absorption anisotropy at and above the energy of the rising edge adheres to the typical $\cos^2$ relationship observed in absorption spectroscopies at other energies, the anisotropy of the pre-edge is far more complicated. Prior studies focusing on pre-edge absorption anisotropy demonstrate a $1\text{-}\cos 4\phi$ dependence of absorption magnitudes with rotation. Experiments presented here show that absorption magnitudes of the pre-edge vary as a function of both electric field vector orientation and wave vector direction. However, rotations around the field vector axis or wave vector axis individually result in $\cos^2$ dependence of absorption magnitudes. Rotations where both wave vector and field vector orientation are varied are not well-fit by either model in the pre-edge. The resulting anisotropy complicates the process of measuring characteristic absorption in the pre-edge, making valence state determinations challenging for strongly anisotropic crystal structures such as pyroxene.

Introduction

In transition metal oxides, absorption over the pre-edge energy range of X-ray absorption spectra is an important indicator of oxidation state and distortion of metal-containing polyhedra. Because of its sensitivity to valence state, the pre-edge has been used by numerous authors to

indicate oxygen fugacity (f_{O2}) of the crystallization or solidification environment of igneous and metamorphic rocks (Bajt et al., 1994; Wilke et al., 2004; Yaxley et al., 2012). Among the community of X-ray absorption spectroscopy (XAS) users, absorption anisotropy of spectra collected from crystals is known to be a barrier to quantifying valence states of multivalent elements (Dyar et al. 2002; Muñoz et al. 2013). Research on mineral samples has shown that in anisotropic materials, calibrations for quantifying multivalent elements can be profoundly affected by the orientation of the photon source relative to the polarization direction of the crystals being studied.

The angular dependence of absorption anisotropy from energies spanning from the rising edge and above is closely approximated as a $\cos^2\theta$ relationship from one absorption magnitude to another. This has been demonstrated by numerous authors (Heald and Stern, 1977; Rosenberg et al., 1986; Stöhr and Outka, 1987) and applied as a way of empirically interpolating absorption magnitudes. In this study, the $\cos^2\theta$ relationship was determined from observations made using ultraviolet-visible (UV-Vis) and infrared spectroscopies, where absorption magnitudes have similar anisotropies.

In our earlier work, Steven et al. (2022) show that absorption anisotropy is well-modeled in three dimensions with a $\cos^2\theta$ absorption indicatrix, a geometric model representing absorption magnitudes for a given field vector direction. However, pre-edge anisotropy was distinctly discordant from the $\cos^2\theta$ model. The discrepancy was suspected to be due to the nature of the quadrupole transitions at pre-edge energies coupled with the relatively low absorption intensities near the intense rising edge. For example, even a slightly overabsorbed scan causes pre-edge peaks to be systematically more intense than an ideal scan, and is not always fully corrected for in the normalization process. The suggestion that the discordance is

the result of quadrupole transitions is not new. An earlier example is a model employed by Hahn et al. (1982), $\sin^2 2\phi$, which interpolates the observed data in Cu K-edge scans of a $(CuCl_4)^{2-}$ complex. Similarly, Uozumi et al. (1992) employed an equivalent model, $1-\cos 4\phi$, to describe pre-edge anisotropy of Ti K-edge spectra of TiO_2.

The objective of this research is to characterize the nature of absorption anisotropy in clinopyroxene, with a focus on the pre-edge. Geologically, clinopyroxenes are an important index mineral for determining conditions of the crystallization environment, namely in geothermobarometry and oxybarometery. Among anisotropic minerals, clinopyroxenes exhibit extreme X-ray absorption anisotropy, making them an ideal candidate for examining the angular dependence of absorption anisotropy. Although the pre-edge peaks are the focus of these experiments, full spectra were collected to gauge the extent of over-absorption. These experiments were run on samples of end-member Fe^{2+} and Fe^{3+} clinopyroxenes, as well as a mixed Fe^{2+}/Fe^{3+} sample.

Background

In spectra acquired over visible wavelengths, anisotropic absorption is routinely observed as pleochroism on a polarized light microscope. The amount of absorption depends on absorber concentration, absorber orientation, and the orientation of vibration directions in the viewing section of the crystal. In other words, given a random section of a crystal, the amount of absorption is first dictated by the optical indicatrix and its orientation, then by the absorption indicatrix at a given wavelength. Examples of the interplay between optical and absorption indicatrices are given in Libowitzky and Rossman (1996) applied to infrared spectroscopy. The orientation of vibration directions can be determined if the optical indicatrix orientation is

known. Vibration directions are simply the semi-major and semi-minor axes of an ellipse formed by a plane section across the optical indicatrix. When linearly polarized light is oriented along a vibration direction, a true absorption magnitude can be acquired. Plane sections of ellipsoid calculations are ubiquitous in many corners of science, but an example derivation is in Gendzwill and Stauffer (1981).

Because absorption magnitudes are influenced by polarization, observed magnitudes can vary in an irregular fashion depending on the orientation of the crystal and the rotation axis. If the rotation axis is a wave vector axis, absorption magnitudes are always $\cos^2\theta$ dependent. Although refraction and crystal polarization effects are nearly nonexistent for X-ray wavelengths, observed absorption anisotropy over the XAS energy range shares some similarities with visible light. To an extent, absorption magnitudes can be modeled in three dimensions using the concept of an absorption indicatrix, where absorption magnitudes in each direction are modeled by a surface-described $\cos^2$ variation in all directions, as seen on the surface in Figure 1 (Steven et al., 2022). However, $\cos^2$ dependence breaks down in the pre-edge. Some authors have employed microscopic models to describe the anisotropy, while others (Hahn et al. 1982; Uozumi et al., 1992) have used a macroscopic 1-cos4ϕ model to describe magnitudes from quadrupole transitions. Based on figures and descriptions of the collection geometries from Hahn et al. (1982) and Uozumi et al. (1992), both collected scans from materials with rotational symmetry, with that axis oriented vertically. The vertical axis was then rotated, designated in both papers as a rotation of ϕ, to collect spectra at various ϕ settings. Those experiments were collected in the geometry equivalent to the position shown in Figure 2, with crystals mounted with rotational symmetry elements parallel to the ϕ-axis, and rotating the spindle axis ϕ. In this study, θ is defined as the rotation axis parallel to the beam direction, and the ϕ-axis is defined as

a rotation axis orthogonal to the beam direction, which can be rotated by θ as depicted in Figure 2.

The 3-D models in Figure 1 only apply if the anisotropy depends on a single axis, such as the electric field vector orientation. If there is wave vector dependence, observed absorption magnitudes can deviate from these models. The experiments in this paper are designed to look for and characterize this variation.

Methods and Samples

Three clinopyroxene samples were used to evaluate anisotropy of samples of that range in $Fe^{3+}/\Sigma Fe$. They are 1) HMM119666, a hedenbergite composition from Broken Hill mines, Yancowinna, New South Wales, Australia which has an $Fe^{3+}/\Sigma Fe$ of 0 and formula of $(Ca_{0.990}Na_{0.002})(Fe^{2+}_{0.834}Mg_{0.045}Mn_{0.147})(Si_{1.989}Al_{0.004})O_6$ 2) DH208, an augite composition from mantle xenoliths from Dish Hill, California, USA which has an $Fe^{3+}/\Sigma Fe$ of 0.36 and formula of $(Ca_{0.810}Na_{0.107})(Fe^{2+}_{0.210}Fe^{3+}_{0.118}Mg_{0.579}Mn_{0.008}Al_{0.118})(Si_{1.751}Al_{0.249})O_6$ and 3) AMNH82544, an aegirine from Langesundsfjord, Norway on loan from the American Museum of Natural History which has an $Fe^{3+}/\Sigma Fe$ of 0.97 and formula of $(Ca_{0.007}Na_{0.961})(Fe^{2+}_{0.026}Fe^{3+}_{0.849}Mg_{0.005}Mn_{0.037}Ti_{0.067}Al_{0.008})(Si_{2.013})O_6$.

Clinopyroxene single crystals were mounted on specimen pins with the spindle axis parallel to a random axis, the **b**-axis, or the vector normal to (100). Crystal orientation was guided by the (110) cleavages during mounting, then crystallographic axes vectors were located using single-crystal X-ray diffraction (SC-XRD). The output orientation matrix from SC-XRD

was then related to the principle optical vectors using the methods described in Steven and Gunter (2020).

For precise **b**-axis mounts, the diagonals of the intersections of the (110) cleavages were mounted parallel to the specimen pin axis, resulting in an axis near either the **b**-axis, or the normal vector to (100). While viewing into the microscope, the specimen pin was turned with the X-ray goniometer fixed at the 0˚ spindle position until the long axis of the crystal (the **c**-axis) was roughly in the plane of view for consistency. Crystals with an orientation matrix indicating that the **b**-axis was within approximately 14˚ of the spindle axis are within range of goniometer arc adjustments. Specimen pins on the X-ray goniometer were then marked to indicate the location of the mounting notch and transferred to the coinciding position of an arc goniometer.

Optical orientations and crystal axes were then determined with spindle stage techniques and EXCELIBR (Steven and Gunter, 2017). Despite the slight discrepancy resulting from the transfer between goniometers, the crystallographic orientation from the SC-XRD should be near the crystallographic orientation determined on the microscope (Figure 3). The Y = **b**-axis orientation is then brought to the spindle axis by numerically minimizing the angle between the spindle axis and the **b**-axis with the operations of the goniometer arcs represented as rotation matrices. In Figure 3, open circles represent the orientation after the goniometer arcs are adjusted so that Y = **b** is parallel to the spindle axis (the -x, +x cartesian axis); this required an up-arc adjustment of -10.7˚ and lo-arc adjustment of -0.2˚ in this example. The beamline geometry is then adjusted to match the microscope cartesian basis.

Fe K-edge spectra were collected at the 13-ID-E undulator-based microprobe at the GeoSoilEnviro-CARS sector, Advanced Photon Source (APS), Argonne National Laboratory, USA. Optical and instrument configuration of the beamline is outlined in Sutton et al. (2017). A

cryogenically-cooled, double-crystal Si(311) monochromator set was used for monochromatic radiation. Beam to sample focusing was performed using a pair of 240 mm long, polished, dynamically-bent silicon mirrors in a Kirkpatrick-Baez (KB) geometry. Beam focus is capable of generating focused spot sizes of approximately 1.5 x 2 μm full-width half maximum, and incident monochromatic flux (I_0) in excess of 6 x 10^{12} photons/second, which is measured in a helium-filled, 200 mm-long ion chamber upstream of KB mirror optics.

Experiments from this research measured fluorescence with a solid-state detector at 90˚ to the X-ray source axis (Figure 2). Fluorescence spectra were collected using a Canberra SXD-7 7 element Si drift detector in conjunction with the high-speed digital spectrometer system Quantum Xpress3. Incident X-ray energy was calibrated on the first derivative peak of Fe, 7110.75 eV, from an Fe metal foil standard (Kraft et al., 1996) and no energy drift was detected throughout the analytical session. X-ray absorption spectra were collected for fluorescence with a collection time of 1 second per step from 7012 to 7104 eV at an energy increment of 2 eV from 7012 to 7104 eV for the background region, 0.1 eV increment from 7104 to 7124 eV for the pre-edge and edge region, 0.5 eV increment from 7124 to 7152 eV for the near edge region, and 5 eV increment 7152 to 7407 eV for the EXAFS region.

A motorized θ-axis and ϕ-axis stage were used to perform the microscope stage and spindle stage rotations to align vectors parallel to the **{{typesetting, here and elsewhere, the arrow goes above the E}}**$E^{\rightarrow}$ field vector, though the wave vector direction $k^{\rightarrow}$ is also known for each crystal (Figure 2). Spectra were normalized and flattened initially in the software Larch (Newville, 2013), and figures of the pre-edge are renormalized near the pre-edge to reduce the effects of overabsorption outliers and focus on anisotropy. Flattened full spectra from 7012 to 7354 eV from this research are provided in the Online Materials[1].

This is the peer-reviewed, final accepted version for American Mineralogist, published by the Mineralogical Society of America.
The published version is subject to change. Cite as Authors (Year) Title. American Mineralogist, in press.
DOI: https://doi.org/10.2138/am-2022-8547. http://www.minsocam.org/

184

185 **Fitting Data**

186

187 Above the pre-edge, anisotropy of XAS is well-characterized as a $\cos^2\theta$ or $\cos^2\phi$
188 relationship from one absorption magnitude to another, as is the case for other absorption
189 spectroscopies (Steven et al., 2022). However, pre-edge peaks are attributed to quadrupole and
190 mixed quadrupole-dipole transitions (De Groot et al., 2009). Because of the quadrupole
191 contributions, interpolating absorption anisotropy in the pre-edge requires a different model. The
192 angular-dependence of quadrupole transitions with respect to ϕ is fit by 1-cos4ϕ following Hahn
193 et al. (1982) and Uozumi et al. (1992). Note that in their experiments, ϕ denotes the angle
194 between $\vec{k}$ and the **a**-axis of TiO_2, where $\vec{k}$ and $\vec{E}$ are kept perpendicular to the **c**-axis.
195 Essentially, those experiments were run by collecting spectra with the **c**-axis of TiO_2 oriented
196 vertically and parallel to the ϕ-axis, and after rotating ϕ at several ϕ angles. The utility of running
197 the experiment in this fashion is that the $\vec{k}$ direction relative to the crystallographic basis is
198 easy to determine if there is angular dependence on $\vec{k}$. In the experiments for this study, ϕ only
199 designates the angle around the axis of the spindle, and crystal orientations are designated
200 separately. Thus, both $\vec{k}$ and $\vec{E}$ dependence are tested separately in ϕ and θ rotations.
201 In two dimensions, the observed $\cos^2\theta$ magnitudes of a section are fit numerically to
202 solve the parameters a, b, and ψ in the expression $a*\cos^2(\theta + \psi) + b*\sin^2(\theta + \psi) = r$, where r is
203 an absorption magnitude. For example, using a Gauss-Newton algorithm for angular-dependent
204 data of spectra collected at 7120 eV, the resulting fit has the parameters a = 0.7506 b = 0.3626 ψ
205 = 8.22° with an RMSE of 0.0136 for the sample in Figure 4. In scans where the $\cos^2$ does not fit

the data alone, a weighted combination of $\cos^2$ and 1-cos4θ dependences are used following the discussion of mixed dipole and quadrupole absorption character in Hahn et al. (1982).

Scan types

Three scan types are used here to test anisotropy with respect to rotating ϕ and θ. The first type includes scans where ϕ is rotated at θ = 0˚, which is denoted as the ϕ-axis, where $E^{\rightarrow}$ // ϕ. These scans are used only to test for wave vector dependence of spectra by fixing the orientation of $E^{\rightarrow}$ relative to the crystal's orientation. The second scan type is a rotation of ϕ at θ = -90˚ (ϕ-axis, $E^{\rightarrow} \perp \phi$). This geometry is inspired by visible light absorption behavior, where if **b** is parallel to the ϕ-axis for a monoclinic crystal, the orthogonal direction is always a vibration direction, eliminating crystal polarization effects.

The final scan type is a rotation of θ, which is also inspired by visible light absorption behavior. This geometry is equivalent to rotating a microscope stage and observing pleochroism. In θ rotations for visible light, there are two orthogonal vibration directions due to polarization through the crystal. Relative to the lower polarizer, absorption magnitudes between the vibration directions arise from the probability of polarization along these two paths rather than absorption probability itself.

All three scan types were acquired on a near end-member Fe^{2+} hedenbergite sample HMM119666. For the endmember Fe^{3+} aegirine samples and the mixed valence augites, only the ϕ-axis, $E^{\rightarrow}$ // ϕ and ϕ-axis, $E^{\rightarrow} \perp \phi$ scans were acquired. In each geometry, a spectrum is collected, then the next spectrum is collected after rotating either the ϕ-axis or θ-axis by 10˚

depending on scan type. This is repeated until a section spanning 0˚ to 170˚ or more is completed.

Results

Hedenbergite ($Fe^{3+}/\Sigma Fe = 0.0$)

Hedenbergite samples (Fe^{2+}-containing only without Fe^{3+}) have three dominant pre-edge peaks centered approximately at 7110.9 eV, 7111.7 eV, and 7113.2 eV. Hedenbergite sample HMM119666 was run in three experimental geometries, two of which were sweeps with $E^{\rightarrow}$ oriented along various axes along (010) and one with $E^{\rightarrow}$. // ϕ-axis // **b**-axis at different angles of ϕ. In the first (010) scan, the crystal was mounted with **c** // ϕ with ϕ turned such that the photon propagation direction $k^{\rightarrow}$ // **b**-axis at various θ settings (Figure 2). The second (010) scan geometry is with the **b**-axis // ϕ at θ = -90˚, while turning to various ϕ settings, and thus, $E^{\rightarrow}$ was also along axes in the (010) plane.

ϕ-axis, $E^{\rightarrow}$ // ϕ // **b**-axis

The ϕ-axis scan with $E^{\rightarrow}$. // ϕ // **b**-axis was run to test if or to what degree is there wave vector dependence of X-ray absorption spectra of clinopyroxenes. HMM119666 was mounted with the spindle axis ϕ parallel to the **b**-axis for both consistency and to cover a wide variety of orientations relative to a known symmetry axis. The scan geometry of this experiment has θ fixed at zero for all spectra with the spindle axis parallel to the polarization axis $E^{\rightarrow}$. Spectra

were collected every 10 degrees from $\phi = 0^{\circ}$ to $\phi = 170^{\circ}$. With $E^{\rightarrow}$ fixed along the b-axis, the angular dependence of absorption relative to the crystal's orientation is with respect to $k^{\rightarrow}$ orientation in this dataset (Figure 6). As demonstrated in Figure 6, pre-edge peaks of hedenbergite have strong absorption anisotropy when $k^{\rightarrow}$ is varied and the orientation of $E^{\rightarrow}$ is fixed relative to the crystal. Spectra are fit with a $\cos^2\phi$ dependence for comparison, based on its coincidence with the data.

θ-axis, $E^{\rightarrow} \perp$ **b**-axis

Absorption magnitudes collected at different settings of θ were used to test whether absorption anisotropy at X-ray wavelengths is analogous to UV-Vis and infrared wavelengths. This geometry is equivalent to observing absorption magnitudes by rotating the microscope stage of a pleochroic mineral in thin section. In this set of experiments, a single crystal of HMM19666 was mounted with the **c**-axis parallel to the ϕ-axis and ϕ was rotated to make $k^{\rightarrow}$ parallel to the **b**-axis at each θ setting. The resulting absorption magnitudes of the prominent pre-edge peaks are plotted relative to θ setting in Figure 7 and fit with $\cos^2\theta$ dependence for comparison. After normalizing, observed absorption anisotropy closely correspond to the $\cos^2\theta$ model for all energies, and the angular dependence of the prominent peak centroids are plotted radially in Figure 7.

ϕ-axis, $E^{\rightarrow} \perp \phi$

The geometry of scans where ϕ is rotated at θ = –90˚ is depicted in Figure 2. In this geometry, the **b**-axis of HMM119666 is mounted parallel to the ϕ-axis and resulted in the absorption magnitudes shown in Figure 8. The orientations of both $k^{\rightarrow}$ and $E^{\rightarrow}$ are varied relative to the crystallographic orientation. They result in a lobed absorption anisotropy relative to the rotation axis minimum and maximum absorption occurring at 45˚ to one another with respect to $k^{\rightarrow}$ and $E^{\rightarrow}$. Only the 7113.2 eV peak can be fit with the 1-cos4ϕ model. The other two peaks are fit with a mixed model using weighted components of both 1-cos4ϕ and $\cos^2\phi$ for comparison.

Augite ($Fe^{3+}/\Sigma Fe = 0.36$)

An intermediate $Fe^{3+}/\Sigma Fe$ concentration of augite, DH208, was analyzed to assess pre-edge peak intensities of a common composition of clinopyroxene. The pre-edge peaks of DH208 is subdivided into centroids centered at 7111.2 eV, 7112.9 eV, 7114.1 eV (Figure 9). Spectra of augite were only collected in the geometry where ϕ is rotated with $E^{\rightarrow}$ perpendicular to ϕ at a fixed θ position of -90˚. This corresponds to the exact position from Figure 2 and collecting spectra every 10˚ from 0-170˚ ϕ. As with the pre-edge absorption of hedenbergite, augite spectra also have the lobed absorption anisotropy when analyzed in this geometry. The peak centered at 7111.2 eV has absorption magnitudes with stronger four-fold symmetry, similar to the 7113.2 eV peak of HMM119666. The 7112.9 eV and 7114.1 eV peaks are not as anisotropic as the 7111.eV peak, but do exhibit nonsystematic differences in absorption intensity when normalized to 7115.5 eV. Peaks are fit with combined $\cos^2\phi$ and 1-cos4ϕ models due to the large discrepancy with both models when applied individually.

296 **Aegirine ($Fe^{3+}/\Sigma Fe = 0.97$)**

297

298 Aegirine samples that are completely oxidized consistently have two dominant pre-edge
299 peaks, one centered at 7112.8 eV and the other centered near 7114.1 eV. Among trivalent
300 transition metal oxides, the general interpretation of the lowest energy peak is that it arises from
301 quadrupole transitions to the empty *d* orbital. The next higher-energy peak has differing
302 interpretations, but is thought to occur from a mix of quadrupole transitions to 3*d* orbital and
303 non-local excitations to an adjacent 4*p* orbital (Vanko et al., 2008). In both scan geometries
304 analyzed, aegirine exhibits the greatest difference in absorption extremes of the pre-edge peaks
305 in all pyroxenes scanned when comparing Figures 6 - 11.

306

307 <u>ϕ-axis, $E^{\rightarrow}$ // ϕ</u>

308

309 A limited dataset was collected in the geometry in which $E^{\rightarrow}$ // ϕ // **b**-axis to investigate
310 whether or not the anisotropy of the Fe^{3+} end-member aegirine is similar to the Fe^{2+} hedenbergite
311 sample. Absorption magnitudes are plotted radially and fit with a $\cos^2\phi$ model in Figure 10. Even
312 with the limited dataset, absorption magnitudes also follow the $\cos^2\phi$ model as with the more-
313 complete dataset of HMM119666. At a minimum, this dataset demonstrates strong absorption
314 anisotropy, and the angular dependence of the absorption anisotropy does not have four-fold
315 symmetry, just as with HMM119666 in this geometry.

316

317 <u>ϕ-axis, $E^{\rightarrow}$ ⊥ ϕ</u>

318

This is the peer-reviewed, final accepted version for American Mineralogist, published by the Mineralogical Society of America.
The published version is subject to change. Cite as Authors (Year) Title. American Mineralogist, in press.
DOI: https://doi.org/10.2138/am-2022-8547. http://www.minsocam.org/

The 7112.8 eV aegirine peak collected in the ϕ-axis, $E^{\rightarrow} \perp \phi$ geometry resembles the same lobed appearance as the 7113.2 eV peak of hedenbergite and the 7111.2 eV peak of augite (Figure 11). The 7114.1 eV peak is only similar to the 7114.1 eV peak of augite but is not particularly well described by either the $\cos^2\phi$ or 1-cos4ϕ models individually. Rather, a mixed model is applied to fit the datapoints following the discussion of mixed quadrupole and dipole transition character among trivalent oxides in Vanko et al. (2008). The pre-edge peaks of aegirine are both the most intense, and most anisotropic in terms of the variation of peak area ratio differences between the 7112.8 and 7114.1 eV peaks with respect to ϕ position.

Discussion

Individually, wave vector dependence appears to be the same as field vector dependence, in that absorption anisotropy is well-fit with the $\cos^2$ model. However, when varying both the wave vector and field vector orientations of any pyroxene crystal, absorption magnitudes delineate irregular patterns that do not always correspond with the 1-cos4ϕ model that worked to describe anisotropy in TiO_2 from Uozumi et al. (1992). Arguably, the combination of the two models describes the absorption anisotropy from Figures 8, 9, and 11 that would coincide with the explanation of mixed dipole and quadrupole character from each sample. Scans analyzing the same section, such as the (010) of HMM119666, exhibit different results depending on rotation and mount axis. For example, with $E^{\rightarrow}$ in the (010) plane, absorption magnitudes collected by rotating ϕ (Figure 8) differs from those collected by rotating θ (Figure 7). This suggests that quadrupole transitions are also strongly dependent on $k^{\rightarrow}$ orientation unlike dipole transitions (Hahn et al., 1982). The results from this study, particularly the scans from HMM119666 are

antithetical to the expected absorption anisotropy if pre-edge peaks resulted from dipole transitions alone. With the selection rules of quadrupole transitions having dependence on $E^{\rightarrow}$ and $k^{\rightarrow}$ orientation (Hahn et al., 1982), the exact scan geometry of the pre-edge is thus a significant factor when analyzing the pre-edge of anisotropic crystals.

Absorption above pre-edge energies does not demonstrate significant variation with respect to $k^{\rightarrow}$ orientation alone (Figure 5). However, the systematic difference in absorption due to differing count rates for each spectrum collected in Figure 5 emphasizes another concern. This concern is the extreme sensitivity of the rising edge to thickness and absorber concentration as discussed in Heald and Stern (1977). Ordinarily, corrections for variation in count rates produce consistent results for multiple spectra collected on irregular crystals. However, overabsorption is likely when analyzing thicker sections of irregular, high Fe crystals such as hedenbergite. As a result, the peaks just above the rising edge are vary in scale, though in a systematic way.

Comparisons between visible light and X-ray absorption

Absorption anisotropy in the pre-edge is only similar to visible light anisotropy in two ways. The first is that rotations around the wave vector axis result in $\cos^2\theta$ dependence of absorption magnitudes. The second similarity is that the pre-edge absorption anisotropy has wave vector orientation dependence. With visible light, this dependence arises from the polarization paths through the crystal, whereas with X-ray wavelengths, the dependence is related to differences in atomic positions along the propagation path, along with the type and nature of the transitions.

When changing the propagation path at a fixed vibration path orientation, there are no perceivable differences in absorption intensity above pre-edge energies. In contrast, pre-edge peak intensities vary by as much as 33% of its maximum intensity when changing the propagation path, even at a fixed $E^{\rightarrow}$ orientation. In visible light spectroscopy, a change in absorption due to propagation path orientation does occur, but is understood to be due to a change in polarization state through the crystal. Because anisotropic crystals are considered to split visible light into two linear vibration paths in classical mechanics, the amount of absorption depends on the amount of light traveling along each path, and the amount of absorption along each path. The amount of light traveling along each path depends on the initial orientation of linearly polarized light relative to the orientations of the two vibration paths. In the XAS experiments above, fluorescence is measured and is proportional to absorption. The disparity between visible light and X-ray absorption anisotropy is strongest when examining pre-edge energies and is only apparent in geometry from Figure 2 where ϕ is rotated. Rotations of ϕ with the rotation axis parallel to the polarization axis at pre-edge energies result in $\cos^2$ angular-dependence. Similarly, rotations of θ also have the $\cos^2$ dependence between pre-edge energies and visible light. As mentioned, the disparity arises from the geometry where ϕ is rotated and $E^{\rightarrow}$ is orthogonal to the ϕ-axis and propagation direction. When modeling the effects of polarization with the optical indicatrix model combined with an absorption indicatrix model of a monoclinic crystal, rotations of ϕ do not result in absorption magnitudes with four-fold symmetry.

Under visible light, ϕ rotations with the geometry of Figure 2 will have two-fold symmetry angular-dependence rather than the four-fold symmetry shown in Figures 8, 9, and 11. Depending on how the crystal is mounted, lower symmetry crystals will generally display two-fold angular-dependence of absorption, which is not necessarily $\cos^2$ dependent in this geometry.

This is the peer-reviewed, final accepted version for American Mineralogist, published by the Mineralogical Society of America.
The published version is subject to change. Cite as Authors (Year) Title. American Mineralogist, in press.
DOI: https://doi.org/10.2138/am-2022-8547. http://www.minsocam.org/

387

388 Possible factors contributing to X-ray absorption anisotropy

389

390 At X-ray wavelengths, diffraction dominates, which has a significant effect on X-ray
391 absorption. For example, the Borrmann effect is the increased X-ray transparency of a crystal
392 along Bragg reflections (Borrmann, 1941).

393 Moreover, quadrupole transitions of the pre-edge have different angular dependence of
394 absorption probabilities than dipole transitions both in theory and observation. As mentioned
395 above, the fits of the pre-edge by Uozumi et al. (1992) from Ti K-edge spectra use the 1-cos4ϕ
396 model. This model fits some of the pre-edge peaks of pyroxenes but not all. It should also be
397 noted that ϕ only refers to the experimental geometry, so the equation is not necessarily
398 applicable to field vector orientations in the crystal's basis. Rather, it may depend on how the
399 crystal is mounted. As shown in Figures 7 and 8, collecting absorption spectra with the field
400 vector oriented along the same axes with differing wave vector directions may yield different
401 results.

402 If X-ray absorption anisotropy was dependent only on the field vector orientation relative
403 to absorbers, there should be no difference in the results shown in Figures 7 and 8, nor should
404 there be variation in the spectra from Figure 10. Further, wave vector dependence is distinct only
405 in the pre-edge of spectra. Differences of absorption anisotropy between quadrupole and dipole
406 transitions are likely the reason for the strong dependence of $k^{\rightarrow}$ orientation for pre-edge
407 energies.

408

409 1-cos4ϕ dependence

This is the peer-reviewed, final accepted version for American Mineralogist, published by the Mineralogical Society of America.
The published version is subject to change. Cite as Authors (Year) Title. American Mineralogist, in press.
DOI: https://doi.org/10.2138/am-2022-8547. http://www.minsocam.org/

410

411 The lobed anisotropy that arises only from the ϕ-axis, $E^{\rightarrow} \perp \phi$ experiments apparently
412 results from the combined wave vector and field vector dependences of the spectra. When
413 spectra are collected at different ϕ-axis settings at ϕ = 0, however, the orientation of $E^{\rightarrow}$ is fixed
414 and the anisotropy follows the $\cos^2$ model. With our limited dataset testing the wave vector
415 dependence of the pre-edge, the absorption magnitudes do not resemble the lobed appearance of
416 the other ϕ-axis scans, and instead correspond closely with the $\cos^2\phi$ fit.
417 Wave vector dependence may arise from a change in multiple scattering paths. In θ
418 rotations, multiple scattering paths are the same relative to the wave vector. Although numerous
419 authors have demonstrated absorption anisotropy of XAS, wave vector and field vector
420 dependence of pre-edge XAS anisotropy was theorized by Brouder (1990) on the basis of
421 multiple-scattering theory combined with group theory.
422 Regardless of whether the wave vector dependence is due to the nature of the quadrupole
423 transitions or a product of multiple scattering paths, the pre-edge is significantly affected by both
424 the orientation of the wave vector and field vector. In experiments where the field vector
425 orientation was fixed and wave vector varied, absorption intensity changed by as much as 33%.
426 This implies that empirical quantification of valence states of anisotropic crystals using the pre-
427 edge is far more complicated than originally thought. Reference datasets for determining redox
428 ratios in anisotropic crystals must account for both contributors to anisotropy. This involves
429 either modeling the anisotropy, or, creating a dataset that is valid for a specific orientation, both
430 in section, and vibration direction.

431

432 **Implications**

433

434 Given the significant wave vector and field vector orientation dependence of XAS on
435 pyroxenes, absorption anisotropy remains difficult to characterize. The fact that anisotropy with
436 respect to wave vector orientation is just as significant as field vector orientation implies that
437 orientation-dependent XAS studies will be most useful if they keep track of $E^{\rightarrow}$ and $k^{\rightarrow}$ in the
438 crystal's basis for each spectrum. The uncertainty of how absorption magnitudes are influenced
439 by orientation has major ramifications for quantifying valence states using the pre-edge only,
440 even in studies attempting to compare similar orientations. In this regard, collecting a spectrum
441 along the same orientation generally refers to the orientation of the field vector, though in XAS,
442 the wave vector axis must also be the same to eliminate the orientation variable in a valence state
443 calibration. Given the change in peak intensity by 33% in some pre-edge peaks, this can
444 dramatically influence Fe valence state predictions in clinopyroxene based on the pre-edge alone,
445 especially if the analyzed orientation does not have the exact same $E^{\rightarrow}$ and $k^{\rightarrow}$ orientation in the
446 crystal's basis. The clinopyroxene group minerals studied here are an extreme example of
447 absorption anisotropy due to the linear arrangement of the absorbers in their structure.

448 More optimistically, this study provides the first steps that will enable modeling for
449 valence state calibrations in pyroxenes empirically. Anisotropy from rising edge energies up
450 follow straightforward systematics once enough datapoints are collected to define characteristic
451 absorption axes (Steven et al., 2022). This allows production of a database of spectra, collected
452 at all possible orientations, to be built from oriented spectra of standards with known Fe^{3+}
453 contents. In other words, acquisition of XAS spectra from standards with known Fe^{2+} and Fe^{3+}
454 concentrations at known orientations provides the data from which spectra at any orientation can
455 now be calculated. Those data can in turn be used as training data for classification or regression

456 models utilizing machine learning algorithms. The resultant models can be used to predict Fe^{2+}
457 and Fe^{3+} in unknown samples at random orientations, either by matching spectra of unknowns to
458 those of standards, or through multivariate analyses based on the training data. Our group is
459 pursuing this approach for pyroxenes, with an ultimate goal of generating robust methodology
460 for measuring Fe^{2+} and Fe^{3+} in pyroxenes in thin section.
461
462 **Funding**
463
464 We are grateful for support of this research from NSF grants EAR-1754261 and EAR-
465 1754268 along with NASA grant 80NSSC19K1008.
466

References

Bajt, S., Sutton, S.R., and Delaney, J.S. (1994). X-ray microprobe analysis of iron oxidation states in silicates and oxides using X-ray absorption near edge structure (XANES). Geochimica et Cosmochimica Acta, 58(23), 5209-5214.

Borrmann, G. (1941). Über Extinktionsdiagramme der Röntgenstrahlen von Quarz. Physikalische Zeitschrift, 42, 157-162.

Brouder, C. (1990). Angular dependence of X-ray absorption spectra. Journal of Physics: Condensed Matter, 2(3), 701.

De Groot, F., Vankó, G., and Glatzel, P. (2009). The 1s x-ray absorption pre-edge structures in transition metal oxides. Journal of Physics: Condensed Matter, 21(10), 104207.

Dyar, M.D., Gunter, M.E., Delaney, J.S., Lanzarotti, A., and Sutton, S.R. (2002). Systematics in the structure and XANES spectra of pyroxenes, amphiboles, and micas as derived from oriented single crystals. The Canadian Mineralogist, 40(5), 1375-1393.

Gendzwill, D.J., and Stauffer, M.R. (1981). Analysis of triaxial ellipsoids: Their shapes, plane sections, and plane projections. Journal of the International Association for Mathematical Geology, 13(2), 135-152.

Glatzel, P., Mirone, A., Eeckhout, S.G., Sikora, M., and Giuli, G. (2008). Orbital hybridization and spin polarization in the resonant 1s photoexcitations of $\alpha{-}Fe_2O_3$. Physical Review B, 77(11), 115133.

Hahn, J.E., Scott, R.A., Hodgson, K.O., Doniach, S., Desjardins, S.R., and Solomon, E.I. (1982). Observation of an electric quadrupole transition in the X-ray absorption spectrum of a Cu (II) complex. Chemical Physics Letters, 88(6), 595-598.

490 Heald, S.M., and Stern, E.A. (1977). Anisotropic X-ray absorption in layered
491 compounds. Physical Review B, 16(12), 5549.
492 Kraft, S., Stümpel, J., Becker, P., and Kuetgens, U. (1996). High resolution x-ray absorption
493 spectroscopy with absolute energy calibration for the determination of absorption edge
494 energies. Review of scientific instruments, 67(3), 681-687.
495 Libowitzky, E., and Rossman, G.R. (1996). Principles of quantitative absorbance measurements
496 in anisotropic crystals. Physics and Chemistry of Minerals, 23(6), 319-327.
497
498 Muñoz, M., Vidal, O., Marcaillou, C., Pascarelli, S., Mathon, O., and Farges, F. (2013). Iron
499 oxidation state in phyllosilicate single crystals using Fe-K pre-edge and XANES
500 spectroscopy: Effects of the linear polarization of the synchrotron X-ray beam. American
501 Mineralogist, 98(7), 1187-1197.
502 Newville, M. (2013). Larch: an analysis package for XAFS and related spectroscopies. In J Phys
503 Conf Ser (Vol. 430, p. 012007).
504 Rosenberg, R.A., Love, P.J., and Rehn, V. (1986). Polarization-dependent C (K) near-edge x-
505 ray-absorption fine structure of graphite. Physical Review B, 33(6), 4034.
506 Steven, C.J., Dyar, M.D., McCanta, M., Newville, M., and Lanzirotti, A. (2022). The absorption
507 indicatrix as an empirical model to describe anisotropy in X-ray absorption spectra of
508 pyroxenes. American Mineralogist: Journal of Earth and Planetary Materials, 107(4),
509 654-663.
510 Steven, C.J., and Gunter, M.E. (2020). EXCALIBR to EXCELIBR and the optical
511 orientation of minerals: Correcting the optical orientation of clinoamphiboles. American
512 Mineralogist: Journal of Earth and Planetary Materials, 105(6), 955-962.

513 Steven, C.J., and Gunter M.E. (2017). EXCELIBR: An Excel Spreadsheet for Solving the
514 Optical Orientation of Uniaxial and Biaxial Crystals. The Microscope 65 (4), 147-152.
515 Stöhr, J., and Outka, D.A. (1987). Determination of molecular orientations on surfaces from the
516 angular dependence of near-edge x-ray-absorption fine-structure spectra. Physical
517 Review B, 36(15), 7891.
518 Sutton, S.R., Lanzirotti, A., Newville, M., Rivers, M.L., Eng, P., and Lefticariu, L. (2017).
519 Spatially resolved elemental analysis, spectroscopy and diffraction at the GSECARS
520 sector at the advanced photon source. Journal of environmental quality, 46(6), 1158-
521 1165.
522 Uozumi, T., Okada, K., Kotani, A., Durmeyer, O., Kappler, J.P., Beaurepaire, E., and
523 Parlebas, J.C. (1992). Experimental and theoretical investigation of the pre-peaks at the
524 Ti K-edge absorption spectra in TiO_2. EPL (Europhysics Letters), 18(1), 85.
525 Vankó, G., de Groot, F.M., Huotari, S., Cava, R. J., Lorenz, T., and Reuther, M. (2008).
526 Intersite 4p-3d hybridization in cobalt oxides: a resonant x-ray emission spectroscopy
527 study. arXiv preprint arXiv:0802.2744.
528 Wilke, M., Partzsch, G.M., Bernhardt, R., and Lattard, D. (2004). Determination of the iron
529 oxidation state in basaltic glasses using XANES at the K-edge. Chemical
530 Geology, 213(1-3), 71-87.
531 Yaxley, G.M., Berry, A.J., Kamenetsky, V.S., Woodland, A.B., and Golovin, A.V. (2012).
532 An oxygen fugacity profile through the Siberian Craton—Fe K-edge XANES
533 determinations of $Fe^{3+}/\sum$ Fe in garnets in peridotite xenoliths from the Udachnaya East
534 kimberlite. Lithos, 140, 142-151.
535

This is the peer-reviewed, final accepted version for American Mineralogist, published by the Mineralogical Society of America.
The published version is subject to change. Cite as Authors (Year) Title. American Mineralogist, in press.
DOI: https://doi.org/10.2138/am-2022-8547. http://www.minsocam.org/

554 **Figures**

555

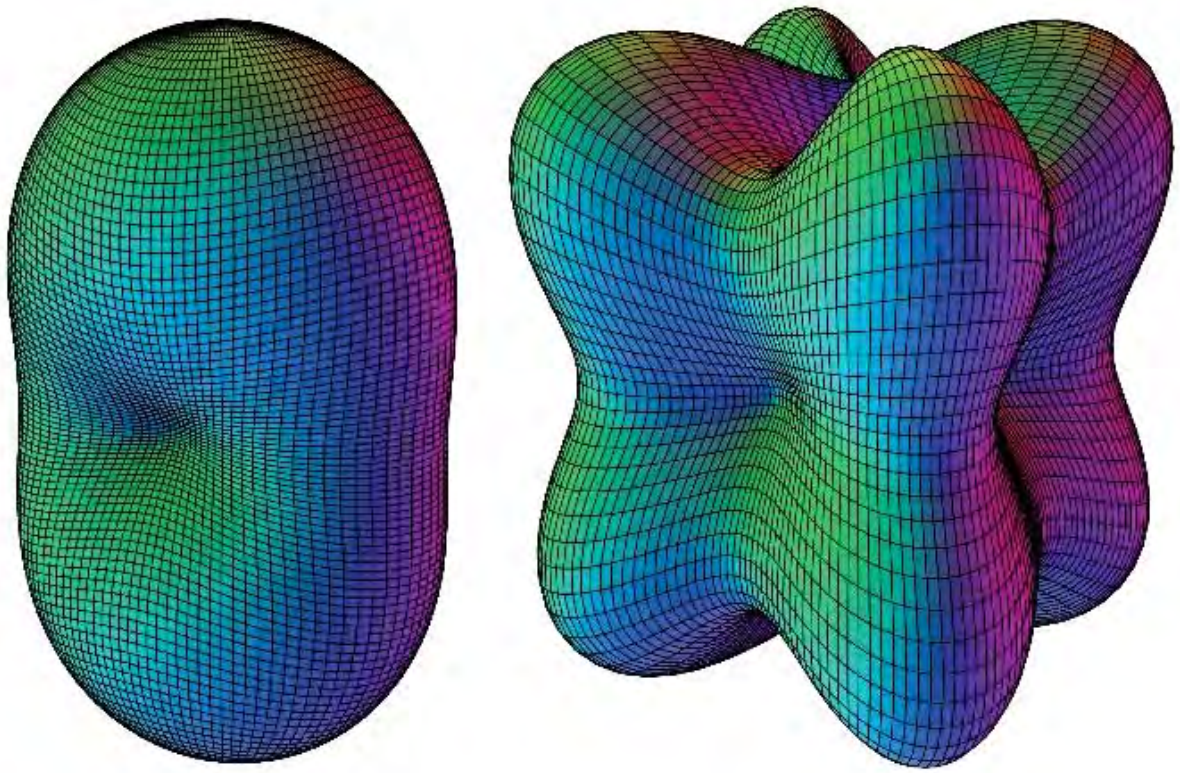

556

557 **Figure 1)** Absorption indicatrices based on absorption due to only dipole transitions (left) and a
558 possible absorption indicatrix due to quadrupole transitions (right).

559

This is the peer-reviewed, final accepted version for American Mineralogist, published by the Mineralogical Society of America.
The published version is subject to change. Cite as Authors (Year) Title. American Mineralogist, in press.
DOI: https://doi.org/10.2138/am-2022-8547. http://www.minsocam.org/

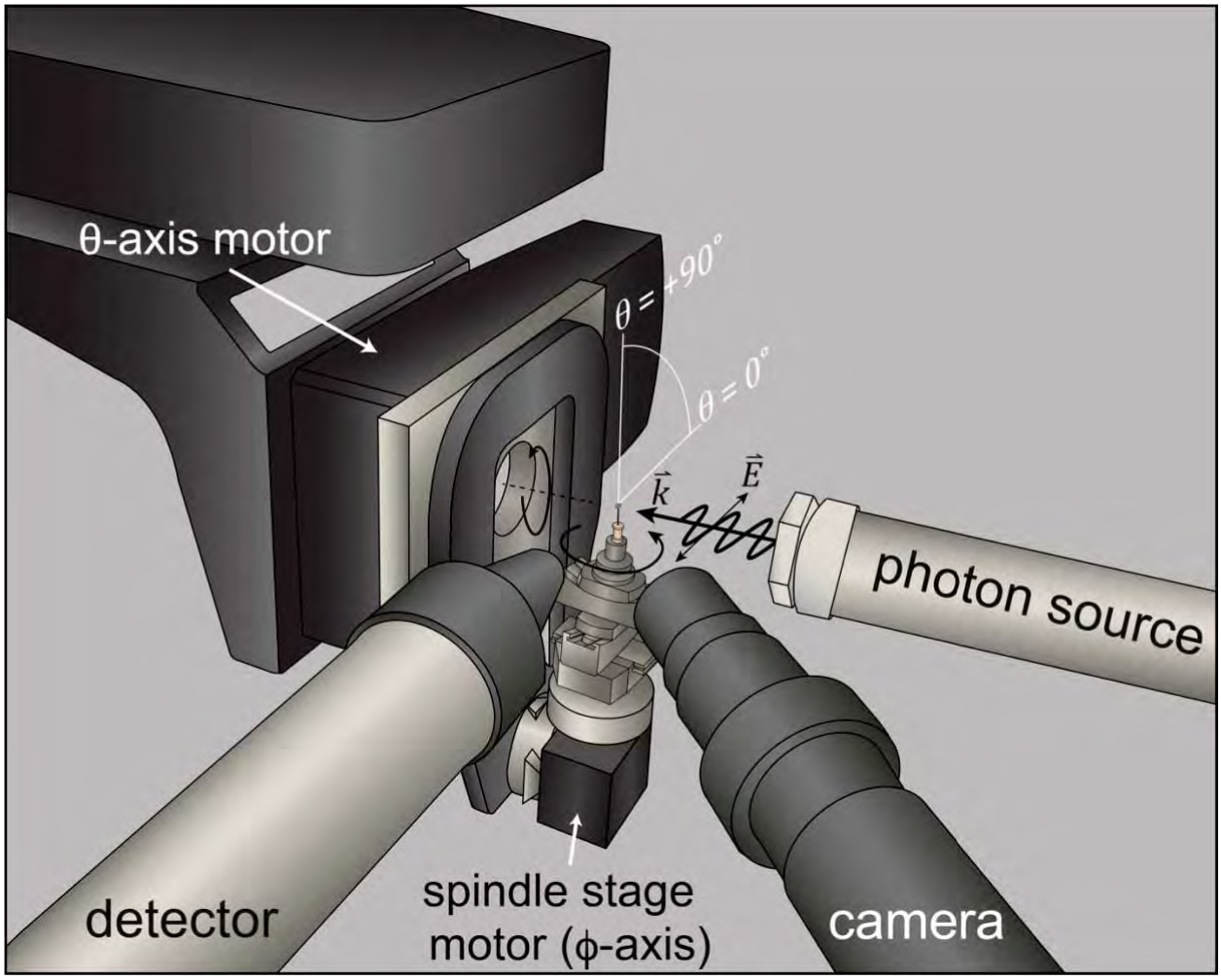

Figure 2) Experimental geometry for analyzing single crystals at Argonne National Laboratory. A motorized spindle ϕ and stage θ rotate around their respective axes. The wave vector $\vec{k}$ of the photon source propagates along the θ-axis and the field vector $\vec{E}$ is orthogonal to $\vec{k}$ and in the horizontal plane.

This is the peer-reviewed, final accepted version for American Mineralogist, published by the Mineralogical Society of America.
The published version is subject to change. Cite as Authors (Year) Title. American Mineralogist, in press.
DOI: https://doi.org/10.2138/am-2022-8547. http://www.minsocam.org/

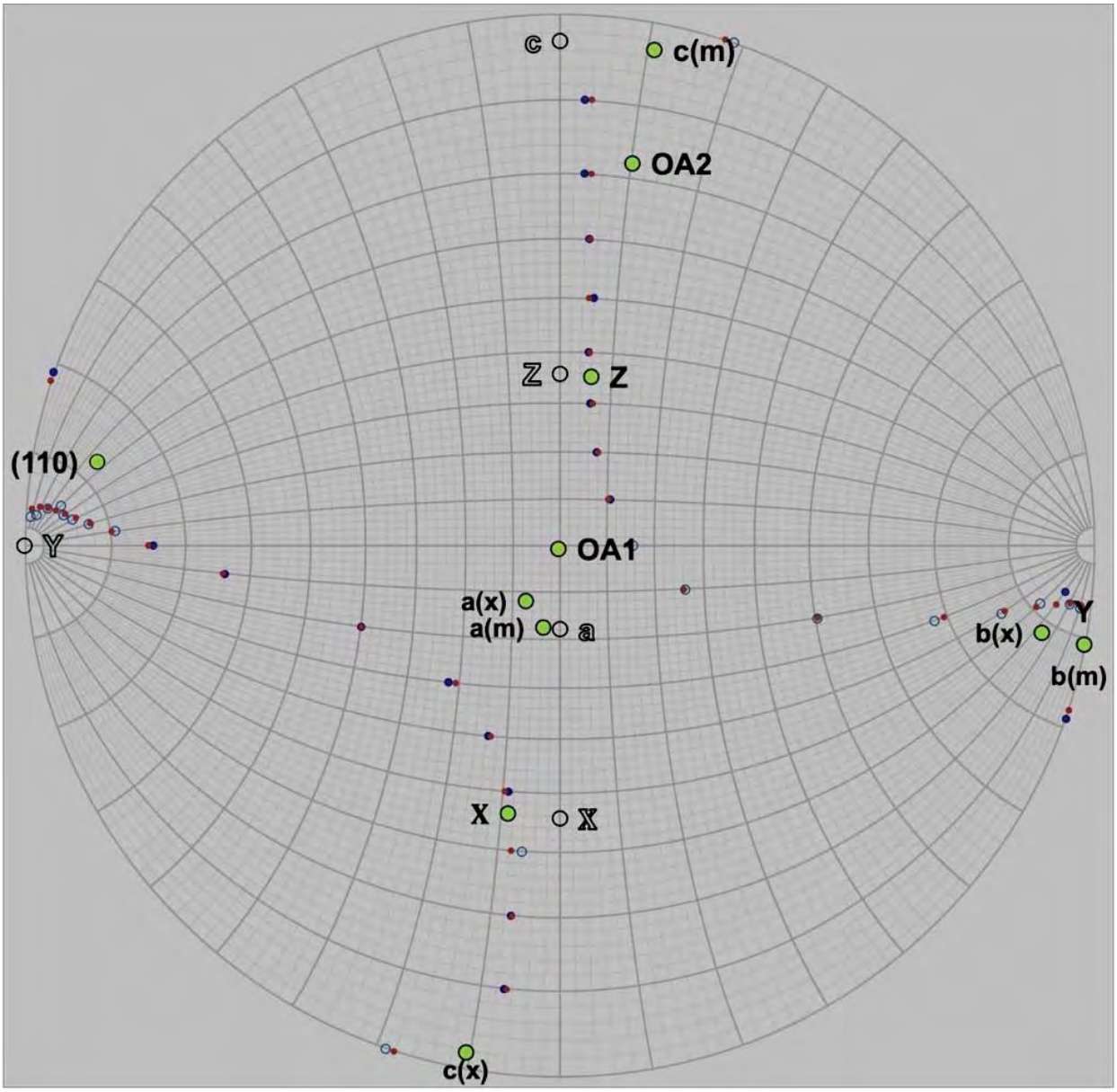

Figure 3) Stereogram of an initial determination of principle optical vectors and crystallographic axes of a pyroxene. The orientation after manipulating the goniometer arcs is represented as open circles.

This is the peer-reviewed, final accepted version for American Mineralogist, published by the Mineralogical Society of America.
The published version is subject to change. Cite as Authors (Year) Title. American Mineralogist, in press.
DOI: https://doi.org/10.2138/am-2022-8547. http://www.minsocam.org/

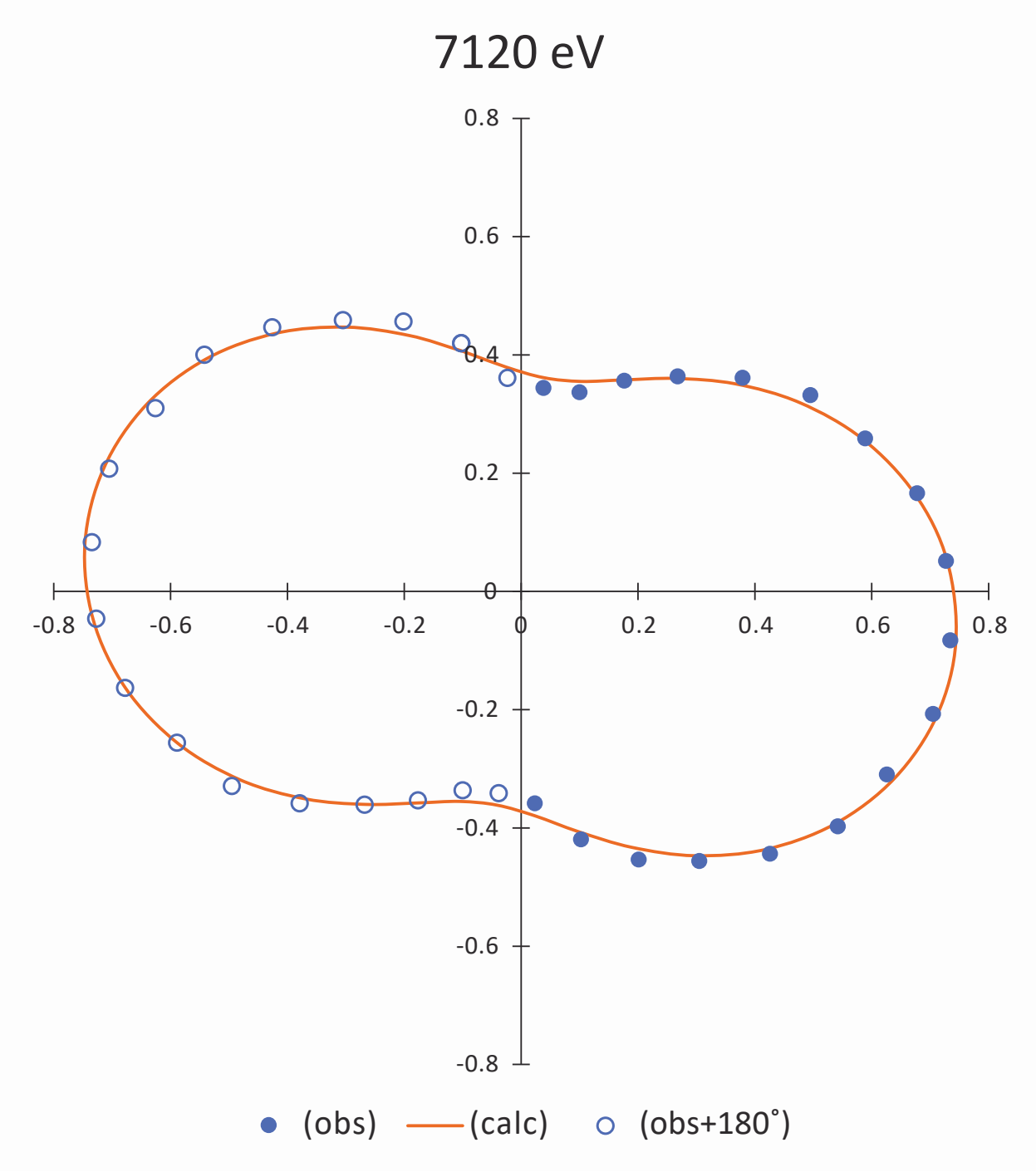

574

575 **Figure 4)** Absorption magnitudes collected at the rising edge (7120 eV) with $\vec{E}$ oriented along
576 various axes in the (010) plane of a 34% $Fe^{3+}/\Sigma Fe$ augite. In this and following figures, the
577 magnitudes of the axes represent absorption intensity.

578

This is the peer-reviewed, final accepted version for American Mineralogist, published by the Mineralogical Society of America.
The published version is subject to change. Cite as Authors (Year) Title. American Mineralogist, in press.
DOI: https://doi.org/10.2138/am-2022-8547. http://www.minsocam.org/

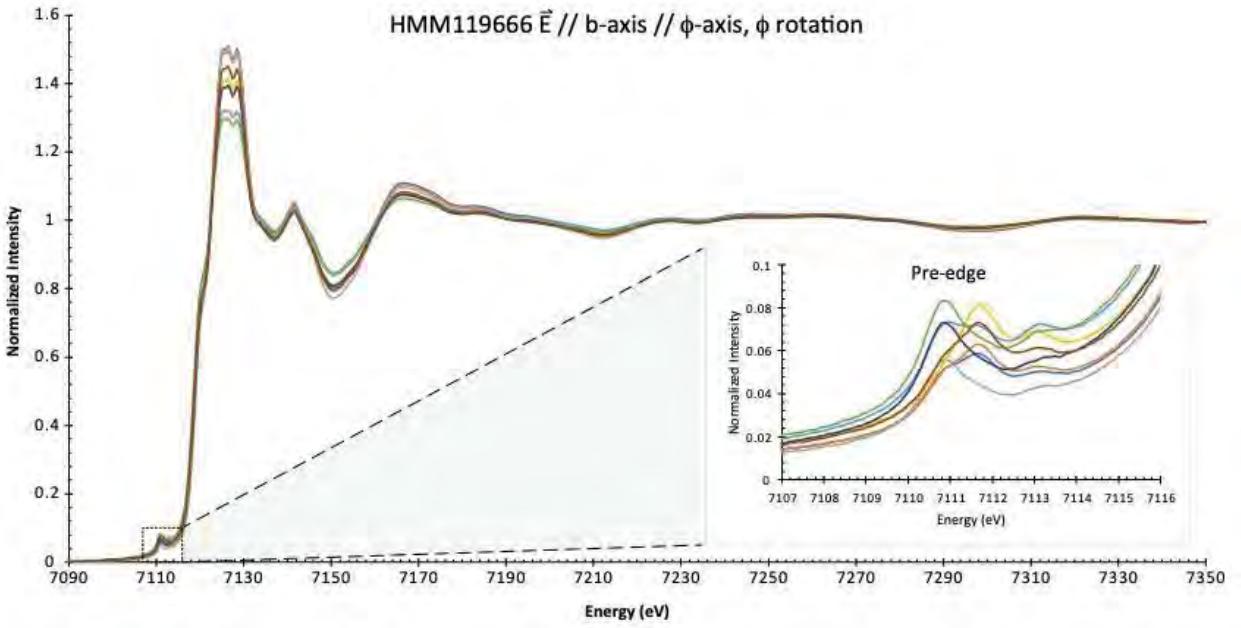

Figure 5) Full X-ray absorption spectra collected from multiple wave vector axes with the field vector axis fixed. A plot of a magnified view of the pre-edge is inset, and a detailed examination of the anisotropy of the pre-edge peak centroids for this sample is given in Figure 6.

This is the peer-reviewed, final accepted version for American Mineralogist, published by the Mineralogical Society of America.
The published version is subject to change. Cite as Authors (Year) Title. American Mineralogist, in press.
DOI: https://doi.org/10.2138/am-2022-8547. http://www.minsocam.org/

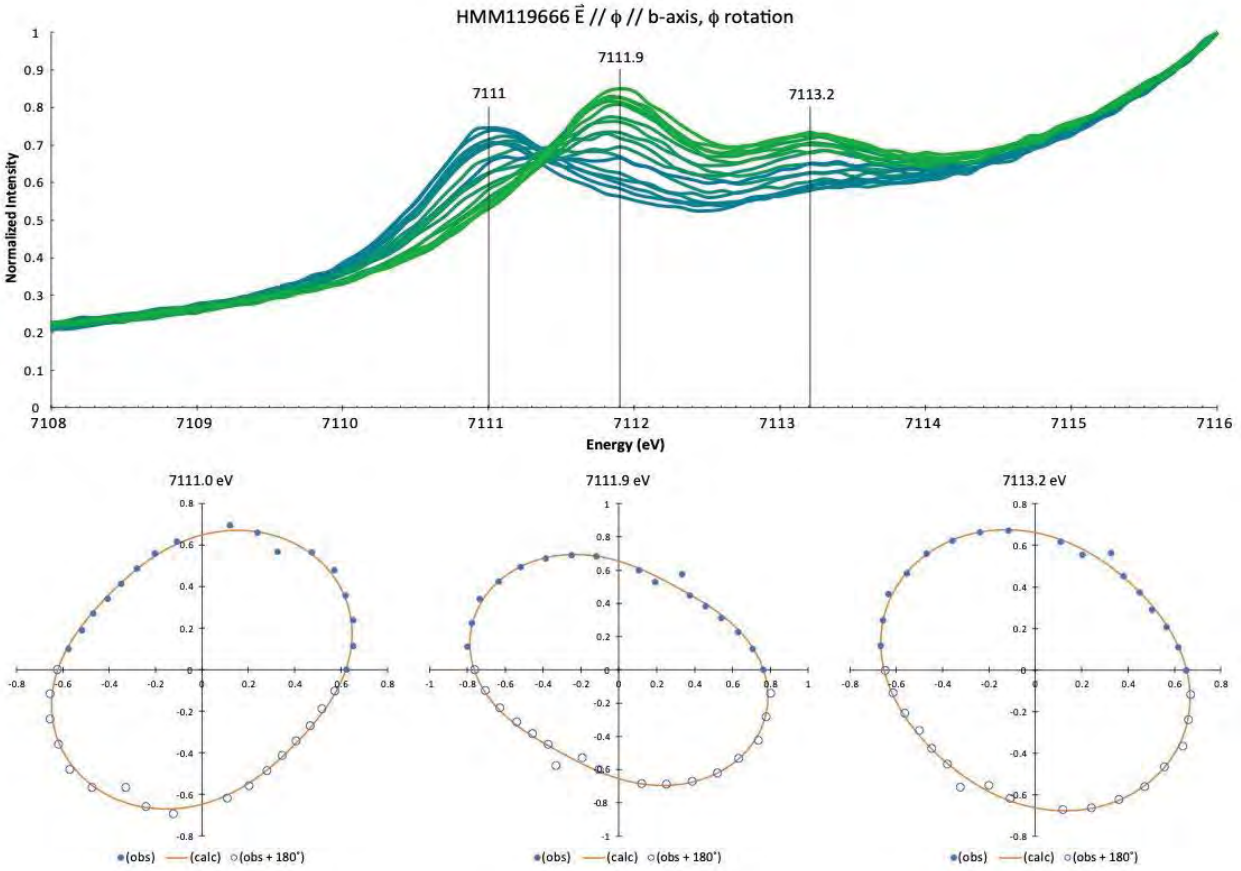

Figure 6) X-ray absorption spectra (top) of a 0.0 $Fe^{3+}/\Sigma Fe$ hedenbergite analyzed at a selection of ϕ-axis angles with $\vec{E}$ // ϕ // **b**-axis. The resulting absorption magnitudes are plotted radially with respect to $\vec{k}$ orientation (bottom) at 7110.8, 7111.7, and 7113.1 eV. Absorption magnitudes are the distances of the points from the origin in the radial plots, and are fit with $\cos^2\phi$ for comparison. Axes in bottom row follow conventions used in Figure 4.

This is the peer-reviewed, final accepted version for American Mineralogist, published by the Mineralogical Society of America.
The published version is subject to change. Cite as Authors (Year) Title. American Mineralogist, in press.
DOI: https://doi.org/10.2138/am-2022-8547. http://www.minsocam.org/

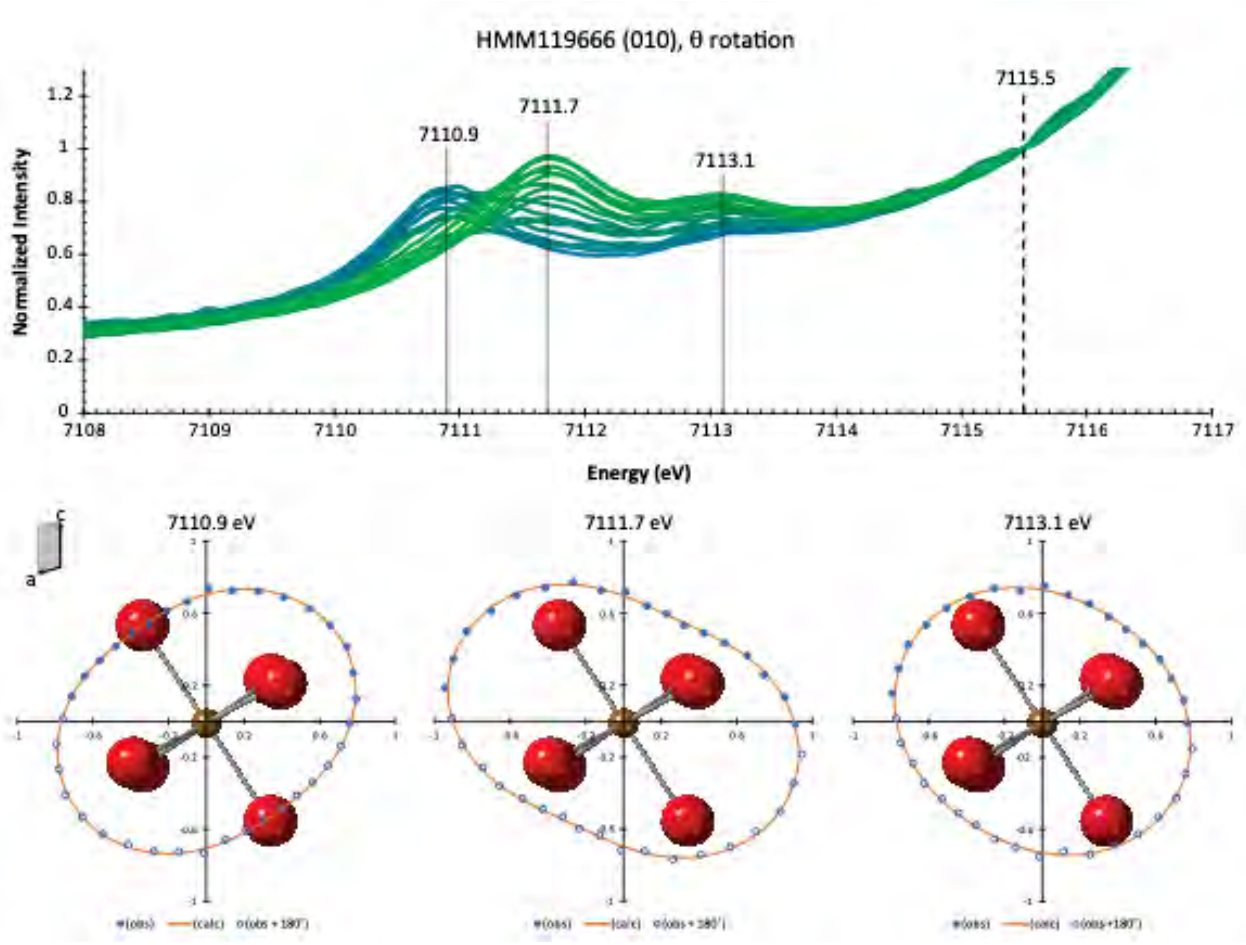

Figure 7) X-ray absorption spectra (top) of a 0.0 $Fe^{3+}/\Sigma Fe$ hedenbergite analyzed with $\vec{E}$ oriented along various axes in (010) with the orientation of $\vec{k}$ fixed along the b-axis. Absorption magnitudes are plotted radially (bottom) with respect to the orientation of $\vec{E}$ at 7110.9, 7111.7, and 7113.1 eV. Spectra are renormalized near the pre-edge peaks at 7115.5 eV to highlight the anisotropy. The orientation of the crystallographic axes and the coordinating polyhedron of the M1 site is depicted relative to the orientation of the absorption magnitudes. Axes in bottom row follow conventions used in Figure 4.

This is the peer-reviewed, final accepted version for American Mineralogist, published by the Mineralogical Society of America.
The published version is subject to change. Cite as Authors (Year) Title. American Mineralogist, in press.
DOI: https://doi.org/10.2138/am-2022-8547. http://www.minsocam.org/

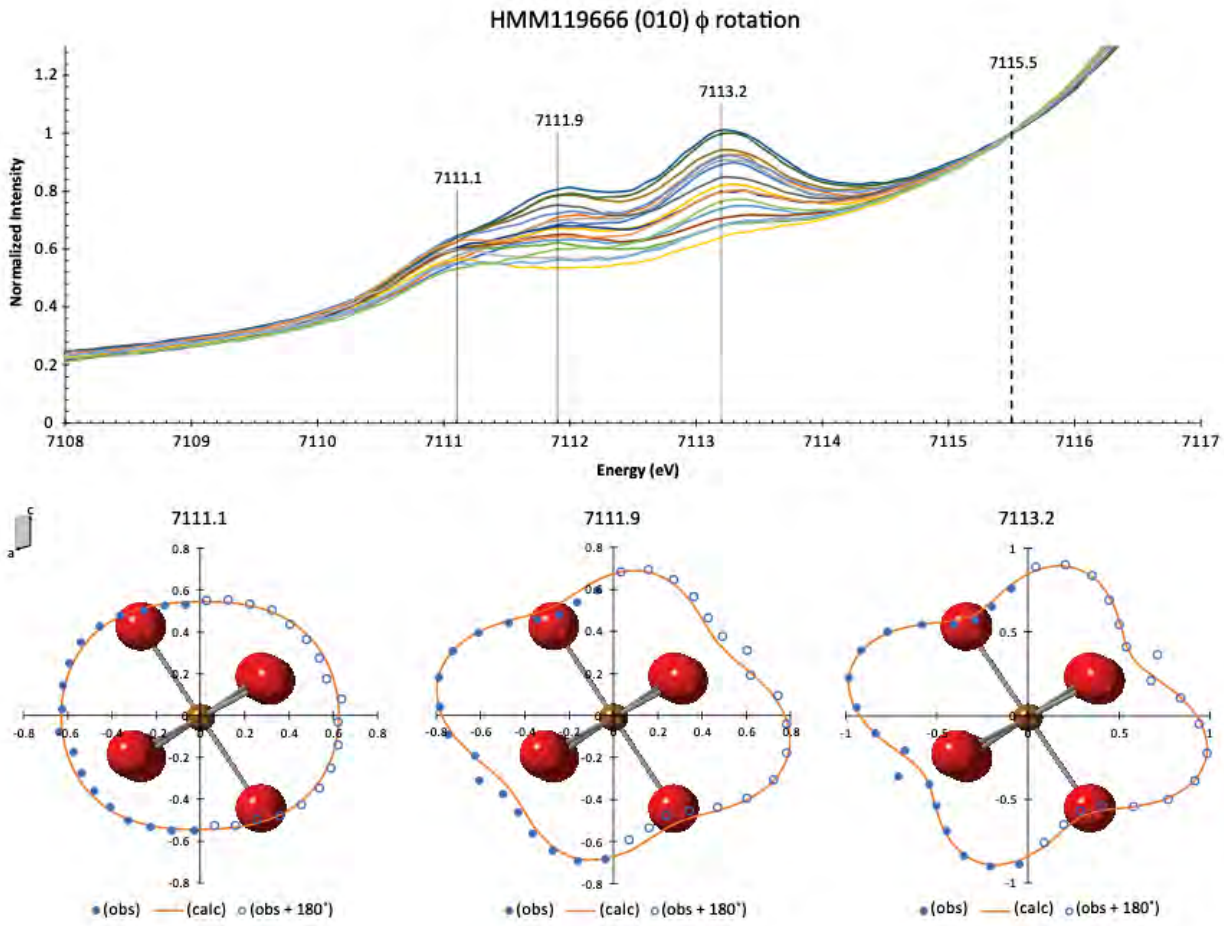

Figure 8) X-ray absorption spectra (top) of a 0.0 $Fe^{3+}/\Sigma Fe$ hedenbergite analyzed with $\vec{E}$ and $\vec{k}$ oriented along various axes in (010). The crystal was mounted with the b-axis // ϕ-axis at θ = -90° as depicted in Figure 2 with spectra collected at various ϕ settings. Absorption magnitudes are plotted radially with respect to $\vec{E}$ orientation, and for each datapoint the orientation of $\vec{k}$ is 90° away. Spectra are renormalized near the pre-edge peaks at 7115.5 eV to highlight the anisotropy. The orientation of the crystallographic axes and the coordinating polyhedron of the M1 site is depicted relative to the orientation of the absorption magnitudes. Axes in bottom row follow conventions used in Figure 4.

This is the peer-reviewed, final accepted version for American Mineralogist, published by the Mineralogical Society of America.
The published version is subject to change. Cite as Authors (Year) Title. American Mineralogist, in press.
DOI: https://doi.org/10.2138/am-2022-8547. http://www.minsocam.org/

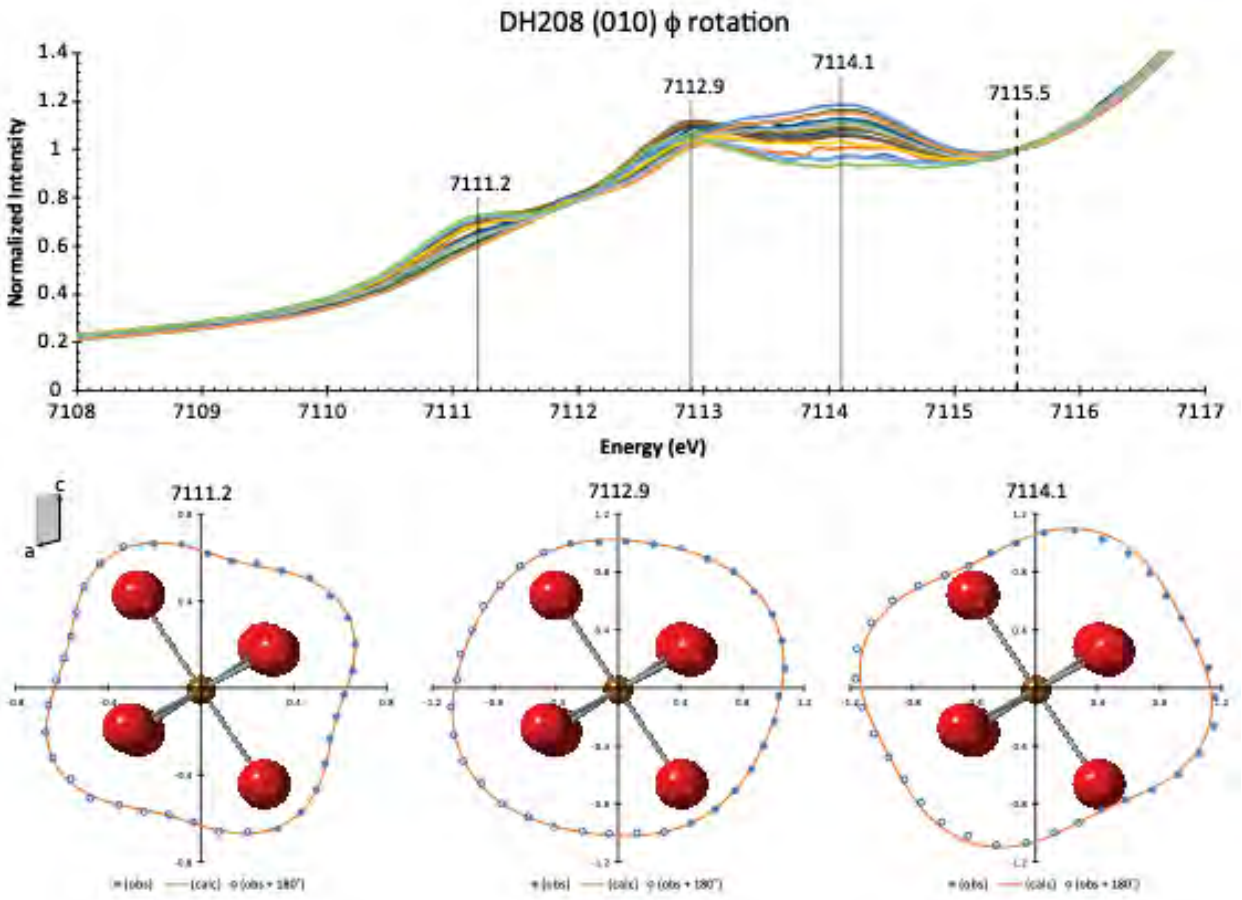

Figure 9) X-ray absorption spectra (top) of a 0.3 $Fe^{3+}/\Sigma Fe$ augite analyzed with $\vec{E}$ and $\vec{k}$ oriented along various axes in (010). The crystal was mounted with the b-axis // ϕ-axis at θ = -90˚ as depicted in Figure 2 with spectra collected at various ϕ settings. Absorption magnitudes are plotted radially with respect to $\vec{E}$ orientation, and for each datapoint the orientation of $\vec{k}$ is 90˚ away. Spectra are renormalized near the pre-edge peaks at 7115.5 eV to highlight the anisotropy. The orientation of the crystallographic axes and the coordinating polyhedron of the M1 site is depicted relative to the orientation of the absorption magnitudes. Axes in bottom row follow conventions used in Figure 4.

This is the peer-reviewed, final accepted version for American Mineralogist, published by the Mineralogical Society of America.
The published version is subject to change. Cite as Authors (Year) Title. American Mineralogist, in press.
DOI: https://doi.org/10.2138/am-2022-8547. http://www.minsocam.org/

623

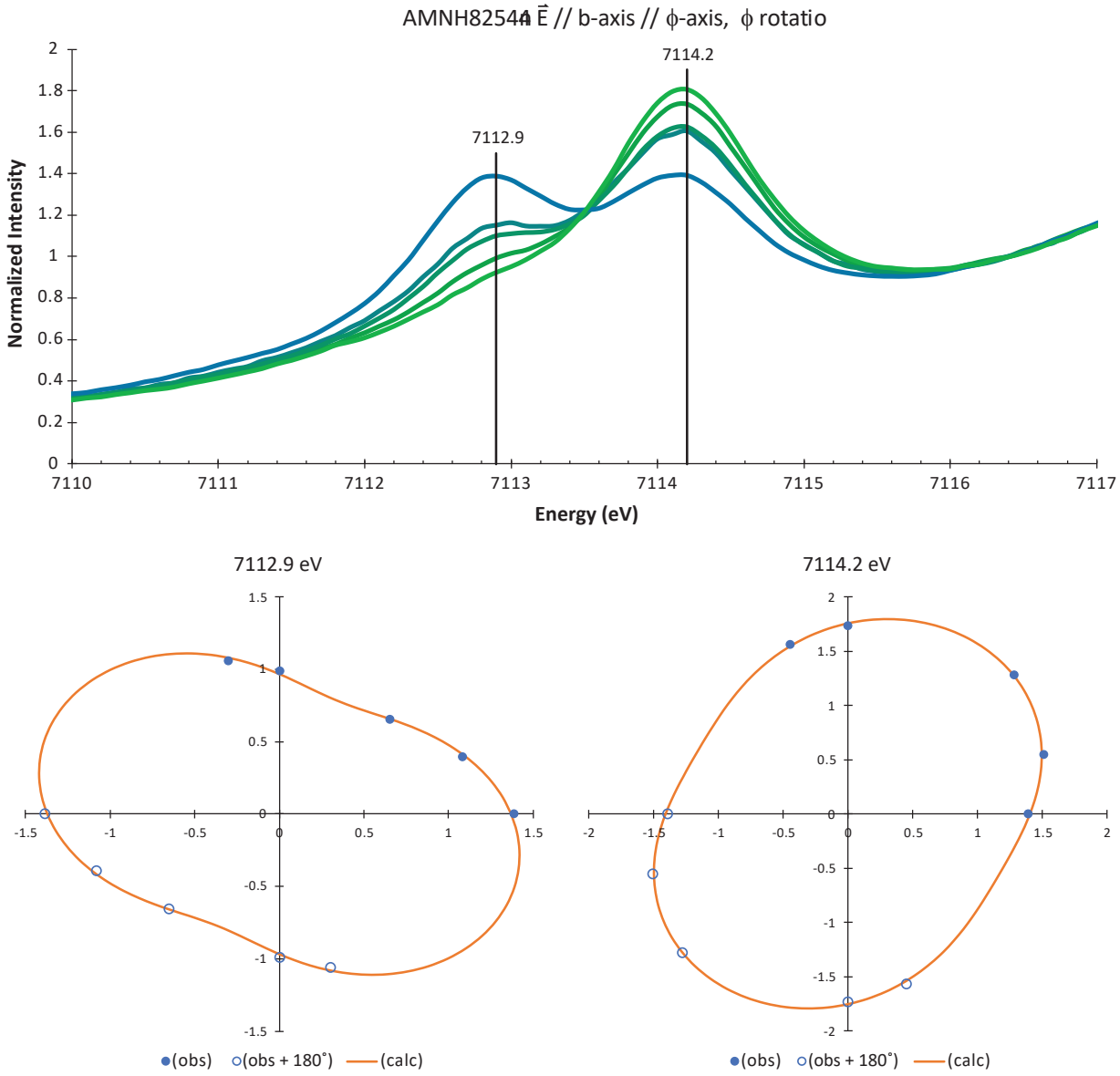

624

625 **Figure 10)** X-ray absorption spectra (top) of a 1.0 $Fe^{3+}/\Sigma Fe$ aegirine analyzed at a selection of ϕ-
626 axis angles with $\vec{E}$ // ϕ // **b**-axis. The resulting absorption magnitudes are plotted radially with
627 respect to $\vec{k}$ orientation (bottom) at 7112.9 and 7114.2 eV. Absorption magnitudes are fit with
628 $\cos^2\phi$ for comparison. Axes in bottom row follow conventions used in Figure 4.

This is the peer-reviewed, final accepted version for American Mineralogist, published by the Mineralogical Society of America.
The published version is subject to change. Cite as Authors (Year) Title. American Mineralogist, in press.
DOI: https://doi.org/10.2138/am-2022-8547. http://www.minsocam.org/

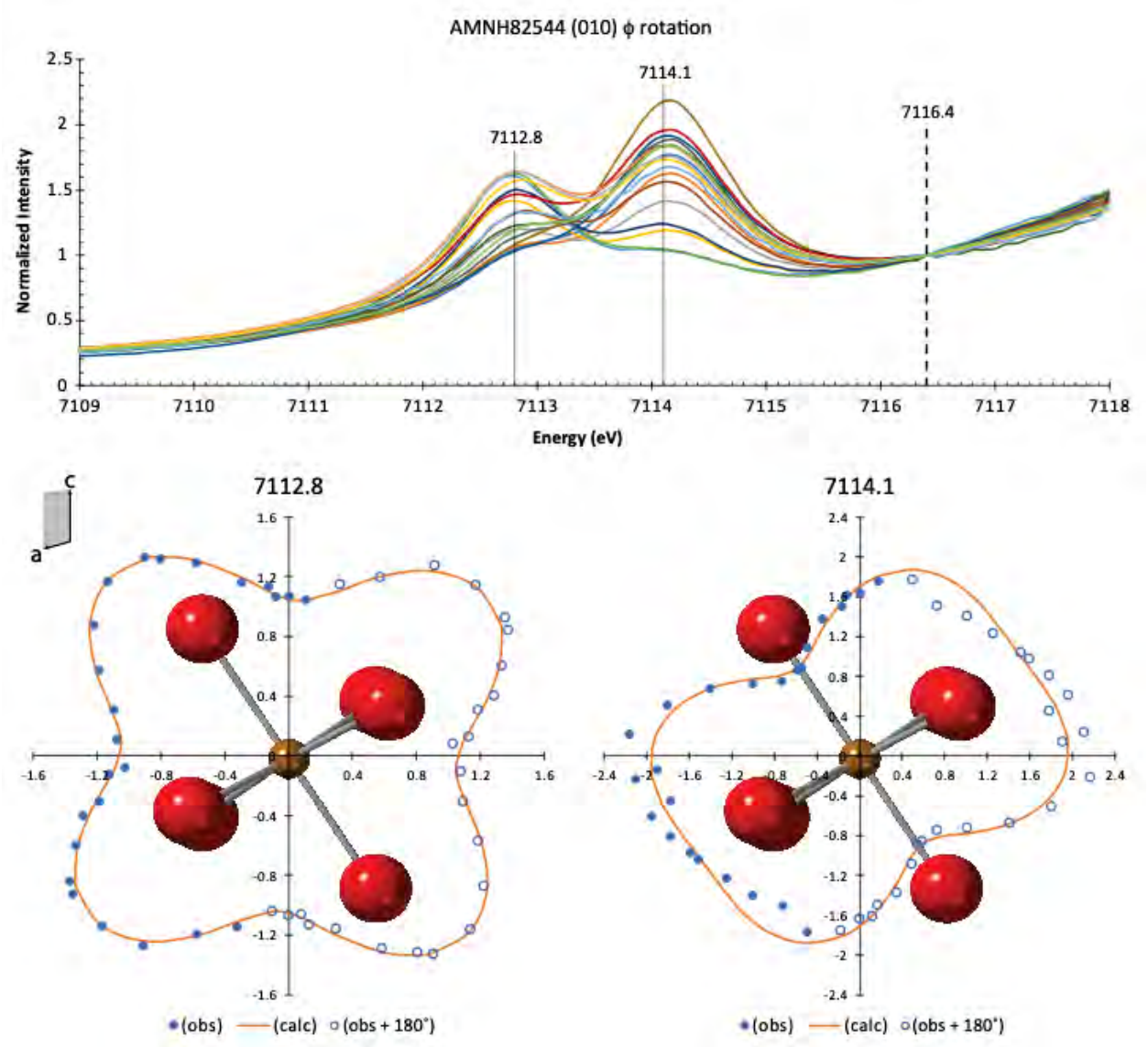

Figure 11) X-ray absorption spectra (top) of a 1.0 $Fe^{3+}/\Sigma Fe$ aegirine analyzed with $\vec{E}$ and $\vec{k}$ oriented along various axes in (010). The crystal was mounted with the b-axis // ϕ-axis at θ = -90° as depicted in Figure 2 with spectra collected at various ϕ settings. Absorption magnitudes are plotted radially with respect to $\vec{E}$ orientation, and for each datapoint the orientation of $\vec{k}$ is 90° away. Spectra are renormalized near the pre-edge peaks at 7116.4 eV to highlight the anisotropy. The orientation of the crystallographic axes and the coordinating polyhedron of the M1 site is depicted relative to the orientation of the absorption magnitudes. Axes in bottom row follow conventions used in Figure 4.